

# Enhancement of non-local exchange near isolated band-crossings in graphene

Jeil Jung<sup>1,\*</sup> and Allan H. MacDonald<sup>1</sup>

<sup>1</sup>*Department of Physics, University of Texas at Austin, USA*

(Dated: June 7, 2022)

The physics of non-local exchange interactions in graphene sheets is studied within a  $\pi$ -orbital tight-binding model using a Hartree-Fock approximation and Coulomb interactions modified at short distances by lattice effects and at large distances by dielectric screening. We use this study to comment on the strong non-locality of exchange effects in systems with isolated band-crossings at energies close to the Fermi energy. We also discuss the role of lattice scale details of the effective Coulomb interaction in determining whether or not broken symmetry states appear at strong interaction strengths, and in determining the character of those states when they do appear.

## I. INTRODUCTION

Graphene sheets are ideal  $sp^2$ -hybridized pure carbon networks, and have attracted attention in recent years because of their appealing combination of theoretical simplicity and exceptional physical properties.<sup>1-4</sup> Most electronic properties of graphene that have been studied experimentally can be successfully described in a non-interacting electron picture.<sup>4</sup> Electron interaction effects are nevertheless clearly manifested in perpendicular magnetic fields where they lead to quantum Hall ferromagnetism<sup>5</sup> and to the fractional Hall effect,<sup>6-8</sup> when two<sup>9,10</sup> or more<sup>11</sup> layers are stacked in a way which leads to flat bands near the Dirac point, and when ribbons with zigzag edges<sup>12</sup> are formed. The strongest interaction effects so far observed in single-layer graphene in the absence of a magnetic field is the logarithmic velocity correction<sup>13-16</sup> at momenta near the Dirac point, now apparent in photoemission measurements<sup>17</sup> and cyclotron mass measurements in suspended graphene.<sup>18</sup> Recent Monte Carlo simulations of zero-field graphene suggest the more interesting possibility of a gap opening<sup>19</sup> at the Dirac point for sufficiently strong interactions, a property that would drastically modify electronic properties. Spontaneous gaps have still not been detected in single-layer samples, even when suspended<sup>7</sup> to reduce disorder and dielectric screening and, although their appearance cannot be fully ruled out for cleaner suspended samples which might become available in the future, likely do not occur.

In this paper we use a  $\pi$ -band lattice-model Hartree-Fock calculation to show explicitly that the logarithmic velocity enhancement is related to non-local exchange interactions with power-law tails. Our calculations provide a numerical estimate of the cut-off length which appears in the argument of the logarithm in the velocity enhancement expression and cannot be obtained from continuum model calculations. We also use our calculation to study the role that lattice scale physics plays in controlling whether or not gapped states can occur in single-layer graphene. We show that the appearance of gapped states is sensitive to the long-range of the Coulomb interaction. By solving self-consistent  $\pi$ -orbital Hartree-Fock equations, we can assess the possibility of realizing topologically non-trivial states like those discussed by Raghu *et al.*,<sup>20</sup> who study an extended Hubbard model with next neighbor interactions.

The paper is organized as follows. We start in section II by briefly explaining our implementation of Hartree-Fock theory for a  $\pi$ -orbital lattice model. Here we define our model Hamiltonian, comment on how we handle complications due to the long-range of the Coulomb interaction, and discuss some other technical details of our calculations. In section III we carry out a detailed study of the power-law non-local exchange interactions and the logarithmic velocity enhancements they produce. In section IV we present a mean-field phase diagram which identifies a variety of distinct broken symmetry solutions and captures the dependence of the competition between them on model parameters. Finally we close the paper in section V with a discussion of our findings and of the general importance of highly non-local exchange interactions in semi-metals or semiconductors with isolated band crossings, or weakly avoided crossings, close to the Fermi level.

## II. $\pi$ -ORBITAL HARTREE-FOCK APPROXIMATION

The simplest tight-binding model for a carbon lattice retains one atomic  $2p_z$  orbital on each lattice site and couples them with nearest neighbor  $pp\pi$  hopping<sup>21</sup> parameters. We use the conventions of Ref. [22], choosing a coordinate system in which the honeycomb's Bravais lattice has primitive vectors

$$\vec{a}_1 = a(1, 0), \quad \vec{a}_2 = a\left(\frac{1}{2}, \frac{\sqrt{3}}{2}\right), \quad (1)$$

where  $a = 2.46\text{\AA}$  is the lattice constant of graphene. The reciprocal lattice vectors are then

$$\vec{b}_1 = \frac{4\pi}{\sqrt{3}a}\left(\frac{\sqrt{3}}{2}, -\frac{1}{2}\right), \quad \vec{b}_2 = \frac{4\pi}{\sqrt{3}a}(0, 1). \quad (2)$$

Because nearest-neighbor hopping connects the honeycomb's two triangular sublattices, the  $2 \times 2$  tight-binding band Hamiltonian is purely off-diagonal:

$$H_0(\mathbf{k}) = \begin{pmatrix} 0 & \gamma_0 f(\mathbf{k}) \\ \gamma_0 f^*(\mathbf{k}) & 0 \end{pmatrix} \quad (3)$$

where  $\gamma_0 = -2.6eV$  is the hopping parameter and the on-site energy has been set to zero. The factor

$$f(\mathbf{k}) = e^{ik_y a / \sqrt{3}} \left( 1 + 2e^{-i3k_x a / 2\sqrt{3}} \cos\left(\frac{k_x a}{2}\right) \right) \quad (4)$$

arises from the phase factors of the Bloch wavefunctions on neighboring sites. We have neglected remote neighbor hopping which gives rise to electron-hole asymmetry, *i.e.* to  $\mathbf{k}$ -dependence of the sum of valence and conduction band energies. The convention for Bloch basis state phase factors which leads to this form of the Hamiltonian is

$$\langle \mathbf{r} | k\lambda \rangle = \psi_{\mathbf{k}\lambda}(\mathbf{r}) = \frac{1}{\sqrt{N_K}} \sum_i e^{i\mathbf{k}(\mathbf{R}_i + \boldsymbol{\tau}_i)} \phi(\mathbf{r} - \mathbf{R}_i - \boldsymbol{\tau}_i) \eta_\sigma \quad (5)$$

where  $\eta_\sigma$  is the spin part of the wavefunction,  $\boldsymbol{\tau}_i$  is the position of sublattice  $l$  in the unit cell, and  $N_K$  is the number of unit cells in the system. The label  $\lambda = (l, \sigma)$  combines the lattice site label  $l$  and the spin label  $\sigma$ .

In this basis the Hartree-Fock Hamiltonian is

$$V_{HF} = \sum_{\mathbf{k}\lambda\lambda'} U_H^{\lambda\lambda'} \left[ \sum_{\mathbf{k}'} \langle c_{\mathbf{k}'\lambda'}^\dagger c_{\mathbf{k}\lambda} \rangle \right] c_{\mathbf{k}\lambda}^\dagger c_{\mathbf{k}\lambda} - \sum_{\mathbf{k}'\lambda\lambda'} U_X^{\lambda\lambda'} (\mathbf{k}' - \mathbf{k}) \langle c_{\mathbf{k}'\lambda'}^\dagger c_{\mathbf{k}\lambda} \rangle c_{\mathbf{k}\lambda}^\dagger c_{\mathbf{k}\lambda'} \quad (6)$$

where (dropping the spin index for simplicity)

$$\begin{aligned} U_H^{\lambda\lambda'} &= \langle \mathbf{k}\lambda\mathbf{k}'\lambda' | V | \mathbf{k}\lambda\mathbf{k}'\lambda' \rangle = \int d\mathbf{r}_1 d\mathbf{r}_2 |\psi_{\mathbf{k}\lambda}(\mathbf{r}_1)|^2 V(|\mathbf{r}_1 - \mathbf{r}_2|) |\psi_{\mathbf{k}'\lambda'}(\mathbf{r}_2)|^2(\mathbf{r}_2) \\ &= \frac{1}{N_K^2} \sum_{i,j} \int d\mathbf{r}_1 d\mathbf{r}_2 |\phi(\mathbf{r}_1 - \mathbf{R}_i - \boldsymbol{\tau}_i)|^2 V(|\mathbf{r}_1 - \mathbf{r}_2|) |\phi(\mathbf{r}_2 - \mathbf{R}_j - \boldsymbol{\tau}_j)|^2 \end{aligned} \quad (7)$$

$$\begin{aligned} U_X^{\lambda\lambda'}(\mathbf{q}) &= \langle \mathbf{k}\lambda\mathbf{k}'\lambda' | V | \mathbf{k}'\lambda\mathbf{k}\lambda' \rangle = \int d\mathbf{r}_1 d\mathbf{r}_2 \psi_{\mathbf{k}\lambda}^*(\mathbf{r}_1) \psi_{\mathbf{k}'\lambda}(\mathbf{r}_1) V(|\mathbf{r}_1 - \mathbf{r}_2|) \psi_{\mathbf{k}'\lambda'}^*(\mathbf{r}_2) \psi_{\mathbf{k}\lambda'}(\mathbf{r}_2) \\ &= \frac{1}{N_K^2} \sum_{i',j'} e^{i(\mathbf{k}' - \mathbf{k})(\mathbf{R}_{i'} + \boldsymbol{\tau}_{i'} - (\mathbf{R}_{j'} + \boldsymbol{\tau}_{j'}))} V(|\mathbf{R}_{i'} + \boldsymbol{\tau}_{i'} - \mathbf{R}_{j'} - \boldsymbol{\tau}_{j'}|) \end{aligned} \quad (8)$$

We can simplify the two-body Coulomb integrals in Eqs. (7) and (8) by combining the momentum-space representation for the Coulomb interaction ( $\tilde{V}^{ll'}(q) = \tilde{V}(q) = 2\pi e^2 / \epsilon_r q$ ) with the atomic orbital form factor  $f(\mathbf{q}) = \int d\mathbf{r} e^{-i\mathbf{q}\cdot\mathbf{r}} |\phi(\mathbf{r})|^2$ . We use the explicit form

$$f(q) = (1 - (r_o q)^2) / ((1 + (r_o q)^2)^4) \quad (9)$$

obtained by Fourier transforming the radial charge distribution of a hydrogenic  $2p$  atomic orbital:

$$\phi(r) = \frac{1}{\sqrt{4\pi}} \frac{1}{\sqrt{24\tilde{a}_o^3/2}} \frac{r}{\tilde{a}_o} e^{-r/2\tilde{a}_o}. \quad (10)$$

The choice  $\tilde{a}_o = a_o / \sqrt{30\text{\AA}}$  reproduces the the covalent bond radius of carbon  $a_o = a / (2\sqrt{3})$ . Calculations in bilayer graphene suggest that a larger effective radius  $\tilde{a}_o = 3a_o / \sqrt{30}$  is a better choice<sup>10</sup> because it accounts crudely for  $sp_2$  bonding orbital polarization. The two-body Coulomb integrals are then given by

$$U_H^{ll'} = \frac{1}{A} \sum_{\mathbf{G}} e^{i\mathbf{G}\cdot(\boldsymbol{\tau}_i - \boldsymbol{\tau}_{i'})} |f(|\mathbf{G}|)|^2 \tilde{V}(|\mathbf{G}|) \quad (11)$$

$$U_X^{ll'}(\mathbf{q}) = \frac{1}{A} \sum_{\mathbf{G}} e^{i\mathbf{G}\cdot(\boldsymbol{\tau}_i - \boldsymbol{\tau}_{i'})} |f(|\mathbf{q} - \mathbf{G}|)|^2 \tilde{V}(|\mathbf{q} - \mathbf{G}|). \quad (12)$$

where  $\mathbf{G}$  are the reciprocal lattice vectors and  $A = N_K A_0$  is the system area.

We will also find it useful to consider an alternate model for interactions which assigns a value,  $V_{\text{eff}}(r)$  to the interaction strength between electrons which depends only on the distance between the lattice sites on which they reside. When expressed in terms of  $V_{\text{eff}}(r)$ ,

$$U_H^{ll'} \simeq \frac{1}{N_K^2} \sum_{i,j} V_{\text{eff}}(|\mathbf{L}_{ij}^{ll'}|) \quad (13)$$

$$U_X^{ll'} \simeq \frac{1}{N_K^2} \sum_{ij} e^{i(\mathbf{k}' - \mathbf{k})\cdot\mathbf{L}_{ij}^{ll'}} V_{\text{eff}}(|\mathbf{L}_{ij}^{ll'}|). \quad (14)$$

For this real space interaction model we use the simple form

$$V_{\text{eff}}(d) = 1 / (\epsilon_r \sqrt{a_o^2 + d^2}). \quad (15)$$

Here  $a_o$  accounts approximately for the reduction of Coulomb interaction strength at short distances due to  $\sigma$  orbital polarization and delocalization of the  $\pi$ -charge density on each lattice site.<sup>23</sup> (In this equation energies are in Hartree ( $e^2/a_B$ ) units and lengths are in units of the Bohr radius  $a_B$ .) In the real space model we choose the on-site interaction parameter  $U$  separately from the longer range tail;  $U$  has been variously estimated as having values between  $U \sim 2\text{eV}$  to  $U \sim 6\text{eV}$ <sup>24</sup>, and up to an effective value of  $U = 9.3\text{eV}$ .<sup>25</sup> While Coulomb interaction energy at the carbon radius length scale is  $\sim 20\text{eV}$ , and an estimate from the first ionization energy and electron affinity of a carbon atom gives  $U = 9.6\text{eV}$ ,<sup>26</sup> the effective on-site interaction strength is expected to be greatly reduced in

the solid state environment because of screening by polarization of bound orbitals on nearby carbon atoms. For larger distance interactions we have included a factor  $1/\epsilon_r$  to account for dielectric screening, as in the momentum space version of the interaction model. The value chosen for  $\epsilon_r$  can be seen as an *ad-hoc* correction for overestimates of exchange interactions in Hartree-Fock theory. We study a range of values for this interaction parameter model but we believe that a value of  $\epsilon_r \sim 4$  is normally appropriate for graphene placed on a dielectric substrate. Values chosen for  $\epsilon_r$  and  $U$  control not only the overall strength of the interaction term<sup>27</sup> but also the relative strength of onsite and long range parts of the interaction. We will show later how this ratio can play a role in selecting the broken symmetry solutions which can appear in these models.

There are two technical difficulties in these calculations, one related to the nature of electron-electron interactions and one related to the electronic structure of graphene. The long-range of the Coulomb interaction creates some numerical difficulties, particularly in evaluating the energies of the charge-density-wave states discussed below. We have found the accurate results can be obtained by choosing a cut-off distance for the  $1/r$  tail so that the coupled sites are as nearly as possible equally distributed between sublattices. The second challenge is related to the band crossing at the Dirac point in graphene, at which the wavefunctions which enter the construction of the exchange potential have a singular dependence on wavevector. Accurate calculations require dense  $k$ -point sampling near the Dirac point, which increases the computational load rapidly in Hartree-Fock calculations because of the non-local exchange interactions. In an effort to achieve a satisfactory compromise between computational load and accuracy we exploit the hexagonal symmetry inherent in the problem. This allows us to limit our calculations to the irreducible wedge with  $1/12$ th of the Brillouin zone area, even though the additional phase factors in the remainder of the zone need still to be properly accounted for when we calculate the exchange potential. We use denser adaptive  $k$ -point sampling near the Dirac cone while keeping a coarser grid in the remainder of the irreducible wedge as shown in Fig. 1. In this way it is possible to achieve good accuracy while maintaining the numerical load at a reasonable level. The coarse  $k$  point sampling region was typically kept to  $16 \times 16$  density while near the Dirac point we have chosen for most of our calculations a sampling density corresponding to  $512 \times 512$  points in the full Brillouin zone and up to  $1024 \times 1024$  density.

### III. NON-LOCAL EXCHANGE AND LOGARITHMIC VELOCITY DIVERGENCE NEAR THE DIRAC POINT

Graphene's Dirac-like low-energy Hamiltonian<sup>1,28</sup> provides an easily studied example of isolated band crossings near the Fermi level of a solid. The band crossing at the two isolated Fermi points introduce singularities in the band Hamiltonian with interesting topological<sup>29</sup> characteristics, and facilitate the application of field-theoretic perturbative methods.<sup>14</sup> As we will discuss later, there are some close analogies between interaction physics in graphene and

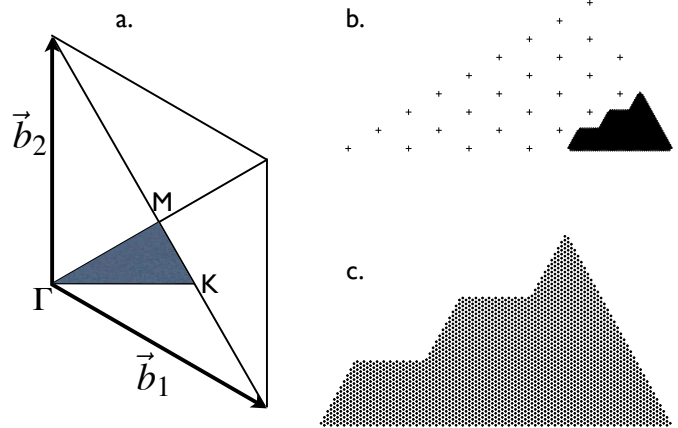


FIG. 1: Choice of the irreducible wedge of the primitive cell (left) and the adaptive sampling of the  $k$ -points in the vicinity of the Dirac point  $K$  used for most of our calculations. The density of  $k$  points in the dense region shown in the figure corresponds to a sampling density of  $512 \times 512$  points.

in gapless<sup>30</sup> and narrow gap<sup>31</sup> semiconductors. It has long been recognized that interaction effects can become prominent in gapless, semimetal, and narrow gap systems. For example in a semimetal with a small overlap between valence and conduction bands, interactions can induce electron-hole pairing and turn the solid into an excitonic insulator.<sup>30,32</sup> In finite gap semiconductors Wannier-Mott excitons can form due to mutual attraction between a hole and an electron. Non-local electron exchange interactions play a relevant role in defining the band structure of narrow band semiconductors.<sup>33</sup> In gapless semiconductors exchange induced corrections in the dispersion relation are large near the crossing point and it has been argued that virtual generation of excitons can lead to a dielectric anomaly.<sup>30,34</sup> A general study of materials with Fermi points has revealed that for linear band crossings, interactions always introduce a logarithmically diverging velocity enhancement,<sup>13</sup> whereas instabilities are expected for quadratic crossings.<sup>13,35</sup>

The marginal Fermi liquid behavior obtained in 3D,<sup>13</sup> and in the graphene 2D case<sup>14</sup> is a consequence of non-local exchange interactions,<sup>15,16</sup> as we discuss at length below. To demonstrate explicitly how these velocity enhancements appear in our calculations we examine the Fock term in Eq. (6) expressed in the sublattice representation:

$$V_X(\mathbf{k}) = \begin{pmatrix} V_X^{AA}(\mathbf{k}) & V_X^{AB}(\mathbf{k}) \\ V_X^{BA}(\mathbf{k}) & V_X^{BB}(\mathbf{k}) \end{pmatrix}. \quad (16)$$

The physics is most clearly explained using the real-space interaction version of our calculations, although the reciprocal-space version is more numerically convenient. The diagonal matrix elements are identical by symmetry and can be expressed using the real space sum of effective two body Coulomb repulsion in Eq. (14). Using the symmetry property that  $\langle c_{\mathbf{k}'A}^\dagger c_{\mathbf{k}A} \rangle = \langle c_{\mathbf{k}'B}^\dagger c_{\mathbf{k}B} \rangle = 1/2$  for every value of  $\mathbf{k}'$

in neutral graphene, we obtain

$$V_X^{AA}(\mathbf{k}) = -\frac{1}{2N_K^2} \sum_{\mathbf{k}, i, j}^{N_K} e^{i(\mathbf{k}'-\mathbf{k})\mathbf{L}_{ij}^{AA}} V_{\text{eff}}(|\mathbf{L}_{ij}^{AA}|) \quad (17)$$

$$= -\frac{1}{2N_K} \sum_{ij}^{N_K} \delta_{i,j} V_{\text{eff}}(|\mathbf{L}_{ij}^{AA}|) = -\frac{U}{2}. \quad (18)$$

At half-filling, particle-hole symmetry implies that the sublattice-diagonal component of the density-matrix is half of the full  $\pi$ -band density-matrix, and therefore diagonal in lattice vector. Only the on-site interaction contributes to  $V_X^{AA}(\mathbf{k})$ . This contribution to the exchange energy is independent of momentum and does not contribute to the quasiparticle velocity. For the off-diagonal term, on the other hand, we use the relation  $\tilde{\rho}_{AB}(\mathbf{k}') = \langle c_{\mathbf{k}'B}^\dagger c_{\mathbf{k}'A} \rangle = -f(\mathbf{k}')/2|f(\mathbf{k}')|$  to obtain

$$V_X^{AB}(\mathbf{k}) = \frac{1}{2N_K^2} \sum_{\mathbf{k}'} \sum_{i,j}^{N_K} e^{i(\mathbf{k}'-\mathbf{k})\mathbf{L}_{ij}^{AB}} V_{\text{eff}}(|\mathbf{L}_{ij}^{AB}|) \frac{f(\mathbf{k}')}{|f(\mathbf{k}')|} \quad (19)$$

$$\equiv \frac{1}{2N_K} \sum_{i,j}^{N_K} e^{-i\mathbf{k}\mathbf{L}_{ij}^{AB}} \rho_{AB}(\mathbf{L}_{ij}^{AB}) V_{\text{eff}}(|\mathbf{L}_{ij}^{AB}|). \quad (20)$$

The second form for the right hand side expresses the exchange self-energy explicitly in terms of the sublattice off-diagonal element of the real-space density matrix:

$$\rho_{AB}(\mathbf{L}_{ij}^{AB}) = \frac{1}{N_K} \sum_{\mathbf{k}'} e^{i\mathbf{k}'\mathbf{L}_{ij}^{AB}} \tilde{\rho}_{AB}(\mathbf{k}'). \quad (21)$$

In momentum space the Dirac band Hamiltonian's sublattice off-diagonal density matrix is singular at the Dirac point because the valence band sublattice pseudospin state changes at the Dirac point. In a 1D model this effect leads to a discontinuity at the Dirac point, in 2D it leads to momentum space vortices, and in 3D to hedgehogs, as illustrated in Fig. 2. Because the function  $f(\mathbf{k})$  vanishes at the Dirac point, the inter-sublattice phase jumps along any line passing through it. When this singularity is Fourier transformed to real space it leads to a slow power law decay, as illustrated in Fig. 3 for the case of graphene, causing the electron exchange interaction to be strongly non-local.

The behavior of the real space tails can be obtained most simply from an analysis of the continuum model. We redefine the wave vector  $\mathbf{k}$  such that it represents the momentum measured from the Dirac point  $\mathbf{K}$ . A general three dimensional Hamiltonian with linear dispersion at an isolated band crossing can be described by the Dirac-Weyl Hamiltonian

$$H(\mathbf{k}) = \hbar v_F \boldsymbol{\sigma} \mathbf{k} = \hbar v_F k \begin{pmatrix} \cos \theta & \sin \theta e^{-i\phi} \\ \sin \theta e^{i\phi} & -\cos \theta \end{pmatrix} \quad (22)$$

where  $\boldsymbol{\sigma} = (\sigma_x, \sigma_y, \sigma_z)$  is the Pauli matrix vector,  $k = \sqrt{k_x^2 + k_y^2 + k_z^2}$ ,  $\tan \theta = \sqrt{k_x^2 + k_y^2}/k_z$  and  $\tan \phi = k_y/k_x$ . The density matrix for the occupied states is then given by

$$\tilde{\rho}(\mathbf{k}) = \frac{1}{2} \begin{pmatrix} (1 - \cos \theta) & -\sin \theta e^{-i\phi} \\ -\sin \theta e^{i\phi} & (1 + \cos \theta) \end{pmatrix} \quad (23)$$

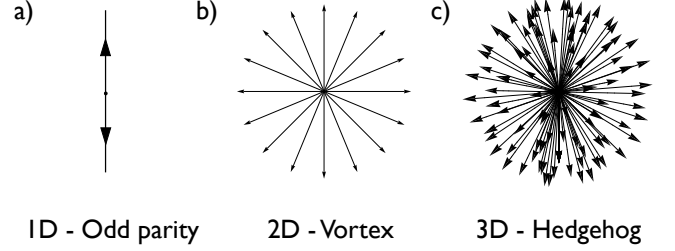


FIG. 2: Illustration of sublattice pseudospin dependence on momentum for the Dirac-like Hamiltonians. In 1D (a) the pseudospin changes direction at the Dirac point, in 2D (b) it has a vortex and in 3D (c) it has a monopole hedgehog structure. In each case the band state sublattice pseudospin changes direction upon crossing through the Dirac point.

The 2D case is obtained by setting  $\theta = \pi/2$  and 1D by setting  $\phi = 0, \pi$ . For  $\mathbf{r} = \mathbf{L}_{ij}^{AB}$  in the  $x$  direction, we obtain the following result for the contribution to the density-matrix from a valley centered at  $\mathbf{K}$ :

$$\begin{aligned} \rho_{AB}(\mathbf{r}) &\simeq e^{i\mathbf{K}\cdot\mathbf{r}} \frac{A_0}{(2\pi)^2} \int_{|\mathbf{k}| < k_c} d\mathbf{k} e^{i\mathbf{k}\mathbf{r}} \tilde{\rho}_{AB}(\mathbf{k}) \\ &\propto \begin{cases} \int_{-k_c}^{k_c} dk \operatorname{sgn}(k) \exp(ikr) & 1D \\ \int_0^{k_c} dk k J_1(kr) & 2D \\ \int_0^{\pi/2} d\theta \int_0^{k_c} dk \sin^2 \theta k^2 J_1(kr \sin \theta) & 3D \end{cases} \\ &\simeq \frac{C_d}{r^d} \end{aligned} \quad (24)$$

where  $d$  is the dimension of the system and  $J_1(x)$  is a Bessel function of the first kind. In graphene similar contributions are made by the two valleys. The dominant contribution to this integral at large  $r$  will come from the non-oscillatory  $kr < 1$  region when  $J_1(x) \sim x/2$ . Inserting this limit into Eq. (24) and integrating up to  $k \sim 1/r$  we see that  $\rho_{AB}(\mathbf{r}) \sim r^{-d}$  at large  $r$ , reminiscent of the dimensional dependence in the decay of Friedel oscillations.<sup>36</sup> The off-diagonal density matrix in other directions differs only by a phase factor.

The slow power law decay behavior of the off-diagonal density matrix in turn leads to a logarithmic divergence in  $\nabla_{\mathbf{k}} V_X^{AB}(\mathbf{k})$  evaluated using Eq. (19) or Eq. (20). We can obtain an approximate form for the exchange potentials in Eq. (20) by changing the sum over discrete lattice sites to be a continuous integral

$$V_X^{AB}(\mathbf{k}) \simeq \frac{1}{2\Omega} \int d\mathbf{r} e^{-i\mathbf{k}\mathbf{r}} \rho_{AB}(\mathbf{r}) V_{\text{eff}}(|\mathbf{r}|) \quad (25)$$

where  $\Omega$  is the volume of the unit cell. Using polar coordinates to represent both  $\mathbf{k}$  and  $\mathbf{r}$  we evaluate the radial deriva-

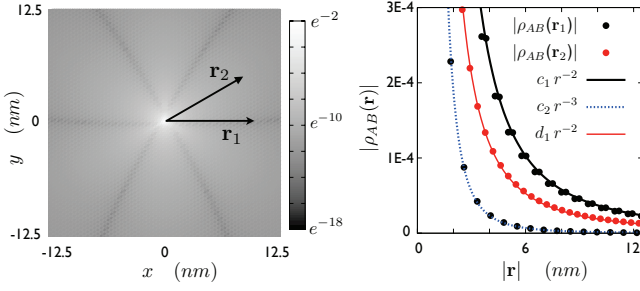


FIG. 3: (Color online) Absolute value of the sublattice off-diagonal density matrix defined in Eq. (21) illustrating the overall power law decay  $r^{-2}$ . *Left Panel:* Grey scale map representation where we can notice a regular anisotropy of the off diagonal density matrix which follows the triangular Bravais lattice structure of graphene. The density matrix element falls off with a larger power law along certain discrete directions. *Right Panel:* Density matrix at discrete lattice vectors along the directions  $\mathbf{r}_1$  and  $\mathbf{r}_2$  indicated in the left panel. For direction  $\mathbf{r}_1$  we notice a periodic dip in the value of  $\rho_{AB}(\mathbf{r})$  every three lattice constants. The density matrix for these lattice vectors has a  $r^{-3}$  decay law. The slow  $r^{-2}$  power law decay reflects the singular dependence of valence band wavefunctions on  $\mathbf{k}$  at the Dirac points. The values of the fitting coefficients are  $c_1 = 0.0037$ ,  $c_2 = 0.0015$  and  $d_1 = 0.0019$  when distances are measured in nm.

tive of the exchange potential to obtain

$$\begin{aligned} \frac{\partial V_X^{AB}(k)}{\partial k} &\simeq \frac{1}{2\Omega} \frac{\partial}{\partial k} \int d\mathbf{r} e^{-i\mathbf{k}\mathbf{r}} \rho_{AB}(\mathbf{r}) V_{\text{eff}}(|\mathbf{r}|) \\ &= \frac{-i}{2\Omega} \int d\mathbf{r} r \cos \tilde{\theta} e^{-i\mathbf{k}\mathbf{r} \cos \tilde{\theta}} \rho_{AB}(\mathbf{r}) V_{\text{eff}}(|\mathbf{r}|) \\ &\simeq C_{\tilde{\theta},d} \int_a^{k^{-1}} dr r^d \frac{1}{r^{d+1}} \propto \ln\left(\frac{1}{ka}\right), \end{aligned} \quad (26)$$

where we integrated the angular variables first, identified the lattice constant as the lower limit of the approximate continuous position integral, and  $k^{-1}$  as the upper limit to avoid the oscillating regime. Note that the space dimension drops out of the final result. Similar conclusions can be reached starting from Eq. (19) and making a multipolar expansion of the Coulomb interaction in momentum space.

In practical calculations both real-space and reciprocal-space Hartree Fock calculations for graphene are able to follow the velocity enhancement only over a limited range of momenta, as illustrated in Fig. 4. The real space formulation used in the present calculation relies on a truncation of the electron interaction range at about six lattice constants, as detailed in the appendix. This prescription is able to describe a large part of the velocity increase due to non-local interactions, but saturates more quickly than the momentum space calculation which fails at small  $k$  values due to the discreteness of the momentum sums used to construct the exchange Hamiltonian.

In Hartree-Fock continuum model calculations, the exchange-enhanced velocity is given by

$$v_{HF} = v_F \left( 1 + \frac{\alpha_{ee}}{4} \ln\left(\frac{p_c}{ka}\right) \right) \quad (27)$$

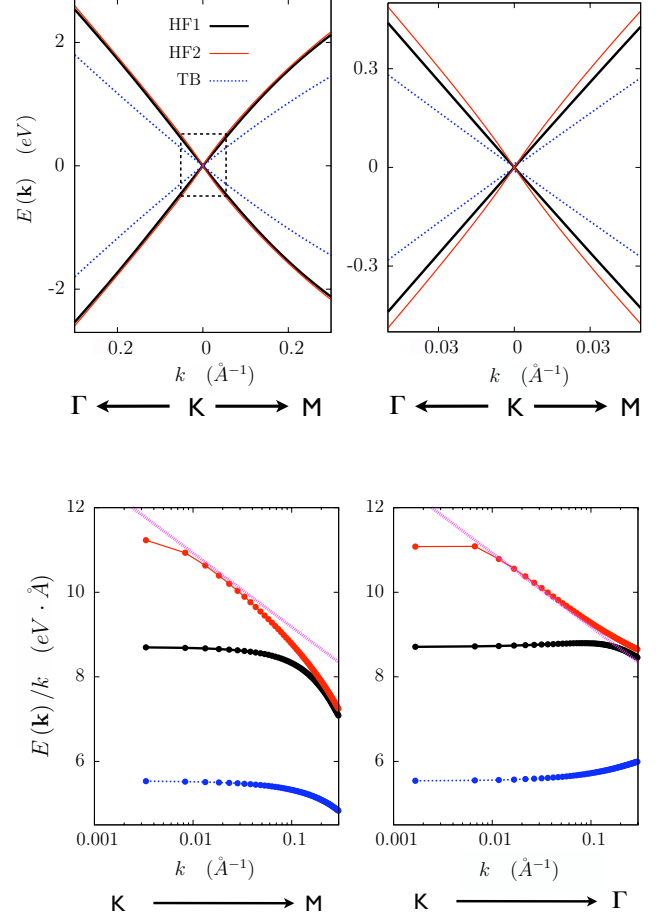


FIG. 4: *Upper panel:* Tight-binding and Hartree-Fock band structures near the Dirac point. The right panels blow up the the small rectangular regions shown in the left panels. We observe that the momentum space Hartree-Fock calculation (HF2) follows the enhancement to smaller momenta than the real space truncated interaction calculation (HF1). *Lower panel:*  $E(k)/k$  versus  $k$  close to the Dirac point. The momentum space HF2 calculation used  $1024 \times 1024$   $k$ -points in the primitive cell. The velocity enhancement saturates in both calculations. The dashed straight line is the small  $k$  fit obtained using Eq. (27) with  $p_c = 30$ .

where  $v_F = \sqrt{3}\gamma_0 a/2$  is the band velocity. The logarithmic enhancement term has the prefactor  $\alpha_{ee}/4$ , where  $\alpha_{ee} = e^2/\epsilon_r \hbar v_F = (c/\epsilon_r v_F)\alpha$ , is the effective fine structure constant,  $c$  is the speed of light, and  $\alpha$  is the ordinary vacuum fine structure constant. Our full Brillouin zone calculation allows us to obtain a numerical value for the dimensionless ultraviolet cutoff parameter  $p_c$  in Eq. (27). By fitting the numerical results we find that  $p_c = 30 \pm 3$ .

#### IV. BROKEN SYMMETRY SOLUTIONS PHASE DIAGRAM

Recent lattice model Monte Carlo studies of interaction effects in graphene carried out by Drut and Lahde<sup>19</sup> predicted that they would be strong enough in suspended graphene samples to induce a CDW broken symmetry state with different electron densities on  $A$  and  $B$  and a gap emerges in the single-particle spectrum. This broken symmetry in graphene is analogous to those that supply mass to elementary particles in particle physics. It now appears clear that these gaps do not occur in experimental samples, possibly because of the role of lattice scale physics that is not reliably modeled in these simulations. Indeed the size of the gaps must be fixed by ultraviolet physics because the two-dimensional Dirac model with Coulomb interaction does not define a characteristic energy scale. The anticipated broken symmetries *do* occur in both lattice and continuum mean-field-theory models of single-layer graphene, although the interaction strengths at which they occur is likely underestimated by mean-field theory. The calculations presented in this section demonstrate that the appearance or absence of these states is sensitive to lattice model detail, in particular to the value of the on-site interaction strength  $U$  and the effective dielectric constant  $\epsilon_r$ . Studies of interactions based on Hubbard models predict antiferromagnetic insulating states which appear for  $U \geq 2.23 |\gamma_0|$  in Hartree-Fock mean-field-theory<sup>37,38</sup> and for  $U \geq (4.5 \pm 0.5) |\gamma_0|$  in Quantum Monte Carlo calculations.<sup>39</sup> A gapped spin-liquid state appears for  $U \simeq 3.5 |\gamma_0|$ ,<sup>40</sup> before the AF state is reached, in the latter case. In graphene, however, any attempt to estimate the character of the ground state must account for longer range interactions.<sup>25,41</sup>

For the analysis carried out in this section we have used the real space formulation of the effective Coulomb interactions given in Eqs. (13-15) that allows a more direct control over the value of the onsite repulsion  $U$  and the Coulomb interaction tail. We used a model with finite truncation of the interaction range with a cutoff radius of about six lattice constants. (Some considerations on optimal cutoff choices are explained in the appendix.) Fig. 5 shows the mean-field phase diagram produced by these calculations in which both spin-density-wave (SDW) and charge-density-wave (CDW) broken symmetry states appear. The solid line in the middle of the paramagnetic region of this figure follows  $\epsilon_r \cdot U = 10.2838$  eV. Along this line the Hartree mean field forming a charge density state with different densities on  $A$  and  $B$  sublattices vanishes. The ordered states which appear above this line are spin-density-wave states, which essentially reflect the physics expected for Hubbard models on a square lattice. The ordered states which appear below this line are charge-density-wave states. For large  $U$  and small  $\epsilon_r$  the charge-density-wave boundary is close to the the  $\epsilon_r \cdot U = 10.2838$  eV line, indicating that its location is determined mainly by this simple competition between short-range and long-range interactions. When this consideration applies, CDW states cannot occur for  $U > 10.2838$  eV since  $\epsilon_r$  cannot take a value smaller than 1. A crude estimate of the onsite repulsion from the carbon atomic radius is  $e^2/a_0 \sim 20$  eV whereas the value of  $U$  that can be ob-

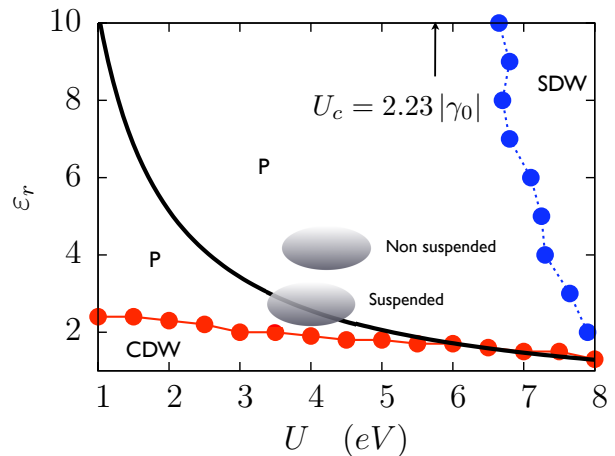


FIG. 5: Phase diagram showing where spin-density-wave (SDW) and charge-density-wave (CDW) broken symmetry solutions appear in our model as a function of the interaction parameters  $U$  and  $\epsilon_r$ . Strong short distance repulsion (large  $U$ ) favors SDW states, whereas weak short distance interactions and strong Coulomb interactions (small  $\epsilon_r$ ) favors CDW states. Below the the solid line in this figure the Hartree mean-field interaction energy is lowered by forming a CDW state which has different densities on  $A$  and  $B$  sublattices. The CDW state boundary lies below this line because the band energy favors uniform densities. The SDW state is a simple antiferromagnet, as expected at large  $U$  on bipartite lattices. The arrow in the figure shows the critical value  $U = 2.23 |\gamma_0|$  beyond which SDW solutions appear for the pure Hubbard model. The shaded regions in the figure indicate the parameter values thought to be most appropriate for graphene sheets that are suspended and for those that are supported by a dielectric substrate.

tained from the first ionization potential and electron affinity of carbon is  $U \sim 9.6$  eV.<sup>26</sup> The actual value will be further reduced when we account for additional screening effects from neighboring and onsite  $\sigma$  orbitals, but the physically appropriate value is highly uncertain. In our phase diagram CDW solutions, which are favored when the longer range part of the interaction is strong but the short-range effective repulsion is weak, are restricted to values of  $\epsilon_r \leq 2.2$  with small enough  $U$ . We conclude from this sensitivity that it is not possible to reliably predict the occurrence or absence of broken symmetry states on the basis of continuum model calculations alone. The values of  $\epsilon_r$  and  $U$  thought to be appropriate based on considerations explained elsewhere<sup>24,25</sup> are consistent with the absence of broken symmetry states in single-layer graphene samples.

#### V. DISCUSSION AND CONCLUSIONS

In the present work we have presented a detailed analysis of mean field Hartree-Fock interaction effects in a lattice model of single-layer graphene. We first analyzed the velocity renormalization of the band dispersion near the Dirac point at the Hartree-Fock level. These calculations demonstrate explic-

itly that the velocity enhancement is produced by non-local exchange interactions between different graphene sublattices and provide a numerical estimate of a dimensionless ultraviolet parameter which cannot be estimated using Dirac continuum model calculations. Similar velocity renormalizations occur whenever a linear band crossing occurs at the Fermi level producing Fermi points. In dimension  $d$  the velocity enhancement is associated with a  $r^{-d}$  power law decay in the real space density matrix. Large velocity enhancements will also occur for similar reasons whenever band gaps are small, or show semimetallic behavior when the character of occupied states varies rapidly on the scale of the Brillouin-zone, although in this case they will always remain finite. This type of physics is responsible for strong the non-locality of exchange interaction in gapless or small gap semiconductors<sup>30</sup> with weak avoided crossing of the bands, in the surface states of topological insulators<sup>42</sup> or in metallic armchair carbon nanotubes.<sup>43</sup>

The velocity enhancements we explore in graphene are partially related to the Fermi surface enhancement incorrectly predicted by Hartree-Fock theory when it is applied to metals.<sup>36</sup> In that case the enhancement is always suppressed by screening. In graphene, however, the density-of-states vanishes at the Fermi level and screening is less effective.<sup>49,50</sup> A random-phase-approximation theory which includes dynamic screening also predicts logarithmic enhancement of the velocity, but with a slightly modified logarithm prefactor.

Our mean field study of broken symmetry states is summarized by the phase diagram as a function of Coulomb interaction parameters in Fig. 5. We have shown that CDW states are favored by weak on-site interactions and or SDW states by strong on-site interactions, but that neither instability occurs in a broad range of interaction parameter space. The most realistic values for the two parameters are still not accurately known, but may be guessed from the character of the broken symmetry states which do in fact occur in the quantum Hall regime of graphene in which the kinetic energy is quenched<sup>44</sup>. Our suggested values for these parameters, both for suspended and unsuspended samples are shown in Fig. 5. According to the phase diagram we have obtained, suspended samples of graphene without substrate dielectric screening ( $\epsilon_r \sim 1$ ) is likely reasonably close to a CDW instability. This result is in rough agreement with the lattice Monte-Carlo calculations of Drut-Lahde<sup>19</sup> who predict a band-gap opening for graphene for a critical value of  $\epsilon_r \sim 1$ . However, the latest available transport measurements for suspended graphene<sup>7</sup> find a finite resistivity of about  $16k\Omega$  in agreement with early predictions<sup>45</sup> for the minimum conductivity for graphene. There is no experimental evidence for an insulating CDW state. This discrepancy between experiment and present theory signals in part the limitations of  $\pi$ -band only models that do not include screening of the bare electron by carbon  $\sigma$  band polarization. An increase of the effective dielectric constant from  $\epsilon_r = 1$  to  $\epsilon_r \sim 2$  to account for screening by degrees-of-freedom not included in the  $\pi$ -band model would be sufficient to explain the absence of broken symmetry states in suspended samples. Recent inelastic X-ray scattering experiments<sup>46</sup> in graphite find screening at high energies

within graphene sheet. These results motivate further efforts to estimate high-energy screening in monolayer graphene.

*Acknowledgments.* We gratefully acknowledge helpful discussions with Dima Pesin. Financial support was received from Welch Foundation grant TBF1473, NRI-SWAN, and DOE grant DE-FG03-02ER45958 from the Division of Materials Sciences and Engineering .

## Appendix A: Real space truncation of the Coulomb interaction

We discuss below the optimum choice for the real-space interaction cutoff. Even though the definition of effective Coulomb integrals in real space has a physically transparent meaning, one important drawback is that the long range of the Coulomb repulsion makes sums over lattice sites of Eqs. (13) and (14) have slow convergence. A simpler method than the more accurate Ewald sum<sup>47</sup> consists in introducing a finite spherical truncation of the electron interaction range<sup>48</sup> as an extended Hubbard model where we incorporate farther neighbor contributions in the Coulomb term. For many purposes this method yields correct enough answers because the effective reach of the Coulomb interaction shrinks when the positive background charge is taken into account. Because of the slower decay in real space of the direct Coulomb term compared to the exchange potential the inaccuracy in the electrostatic energy is usually the largest source of error of this truncation method specially when there is no charge neutrality within the interaction cutoff range in presence of inhomogeneous density distributions. One way to minimize this error is to choose the cutoff range such that the electrostatic energy is minimized in presence of an symmetric charge imbalance in the A and B sublattices of graphene. In order to evaluate the

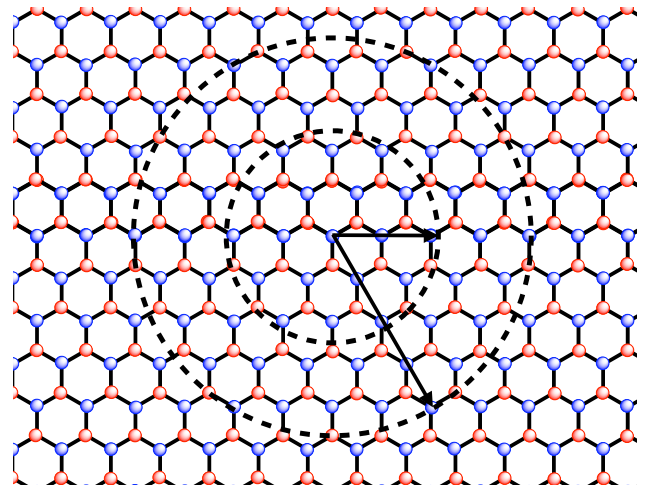


FIG. 6: Real space truncation of the interaction range in graphene as illustrated with two different cutoff values of  $L_{max} \sim 2a$  and  $L_{max} \sim 5a$ . As we change the value of the cutoff radius  $L_{max}$  there are oscillations in the relative number of carbon lattice sites A and B enclosed within the cutoff distance.

cutoff for the Coulomb interaction term that minimizes the er-

ror we express the Hartree energy of a CDW state

$$E_H = \frac{1}{2} \int d\mathbf{r} d\mathbf{r}' \frac{n(\mathbf{r})n(\mathbf{r}')}{|\mathbf{r}-\mathbf{r}'|} \simeq \frac{1}{2} \sum_{i,j} n_i n_j V_{ij} \quad (\text{A1})$$

where we use the notation  $V_{ij} = V_{\text{eff}}(d_{ij})$  for simplicity where  $d_{ij}$  is the distance between the lattice sites  $i$  and  $j$ . Let us consider a charge density transfer of  $\delta n$  from lattice B to lattice A such that the densities are  $n_A = n_0 + \delta n$  and  $n_B = n_0 - \delta n$ . In that case we obtain

$$E_H = \frac{1}{2} \sum_{i \in A, j \in A} V_{ij} (n_0 + \delta n)(n_0 + \delta n) \quad (\text{A2})$$

$$+ \frac{1}{2} \sum_{i \in B, j \in B} V_{ij} (n_0 - \delta n)(n_0 - \delta n) \quad (\text{A3})$$

$$+ \frac{1}{2} \sum_{i \in A, j \in B} V_{ij} (n_0 + \delta n)(n_0 - \delta n) \quad (\text{A4})$$

$$+ \frac{1}{2} \sum_{i \in B, j \in A} V_{ij} (n_0 - \delta n)(n_0 + \delta n). \quad (\text{A5})$$

The linear terms in  $\delta n$  above cancel each other and if we

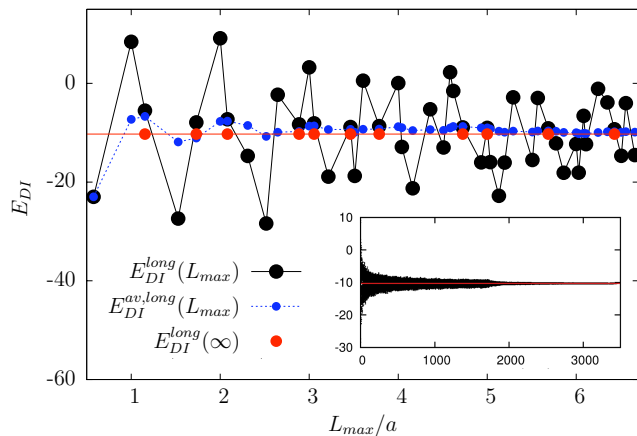


FIG. 7: Longer ranged contributions to the Hartree energy  $E_{DI}^{long}(L_{max})$  as defined in Eq. (A7) which shows a strong cutoff distance  $L_{max}$  dependent oscillation that converges slowly to the limiting value represented with the horizontal line whose behavior is more clearly shown in the inset. We can notice that  $E_{DI}^{long}(L_{max})$  is rather close to the asymptotic limit for certain values of  $L_{max}$ . A better estimate of the asymptotic limit can be obtained from the behavior of  $E_{DI}^{av, long}(L_{max})$  defined in the text.

neglect a constant shift in the origin the electrostatic energy difference per lattice is

$$\delta E_{DI} = \frac{(\delta n)^2}{2} \left[ U + \sum_{j \in A} V_{ij} - \sum_{j \in B} V_{ij} \right] \quad (\text{A6})$$

where  $d_{ij}$  is the distance between lattice sites  $i$  and  $j$ ,  $U = V(d_{ii})$  and  $i$  is a fixed label belonging to sublattice A. We denote the cutoff dependent direct energy corresponding to the long ranged part of the Coulomb interaction as

$$E_{DI}^{long}(L_{max}) = \sum_{j \in A, L_{max}} V_{ij} - \sum_{j \in B, L_{max}} V_{ij} \quad (\text{A7})$$

which shows an oscillatory dependence on the cutoff distance  $L_{max} > d_{ij}$  as represented in Fig. 7. This behavior poses some caveats in extended Hubbard models with only one or two neighbor Coulomb interactions when used for obtaining a phase diagram of broken symmetry states involving charge density modulations or comparing results between different models. We can clearly observe that the above mentioned oscillations slowly converge to a constant for very large  $L_{max}$ . A better estimate for the asymptotic value in the limit  $L_{max} \rightarrow \infty$  can be obtained from  $E_{DI}^{av, long}(L_{max}) = \sum_{i=1}^{N_{max}} E_{DI}^{long}(L_{max}, i) / N_{max}$  averaging the values obtained at each discrete  $i^{th}$  nearest neighbor shell cutoff, where  $N_{max}$  is the total number of nearest neighbor shells corresponding to the cutoff distance  $L_{max}$ . We can observe that for certain specific values of  $L_{max}$  the quantity  $E_{DI}^{long}(L_{max})$  is close to  $E_{DI}^{long}(\infty)$ . In table I we represent the values of some of these select cutoff distances which are the ones that minimize the difference in the number of A and B lattices and therefore minimizes the deviation from charge neutrality for a CDW state within the cutoff range. In our calculations we have used a cutoff just above the value  $L_{max} = 6.4291a$  listed in the table.

\* Electronic address: jeil@physics.utexas.edu

1 K. S. Novoselov et al., Nature 438, 197 (2005).

2 Y. Zhang et al., Nature 438, 201 (2005).

3 A. K. Geim and K. S. Novoselov et al., Nature Materials 6, 183 (2007); A. K. Geim and A. H. MacDonald, Physics Today 60, 35 (2007).

4 A. H. Castro-Neto et al., Rev. Mod. Phys. 81, 109162 (2009).

5 Y. Zhang et al., Phys. Rev. Lett. 96, 136806 (2006); K. Nomura and A. H. MacDonald, Phys. Rev. Lett. 96, 256602 (2006).

6 X. Du, I. Skachko, F. Duerr, A. Luican and E. Y. Andrei, Nature 462, 192 (2009).

7 K. I. Bolotin, F. Ghahari, M. D. Shulman, H. L. Stormer and P.

TABLE I: Optimum values of cutoff  $L_{max}$  and the corresponding values of  $E_{long}^{DI}(L_{max})$  which gives the closest estimates to the asymptotic limit  $E_{long}^{DI}(\infty)$  for each period of oscillation. For completeness we also represent  $E_{DI}^{av}(L_{max})$  defined in the text. We denote with the superscript 1 the results obtained with  $a_o = a/(2\sqrt{3})$  in the definition of the effective Coulomb integral in Eq. (15) and superscript 2 the results we would obtain if we used  $a_o = 0$ .

| $L_{max}$ | $E_{DI}^{long,1}$ | $E_{DI}^{av,1}$ | $E_{DI}^{long,2}$ | $E_{DI}^{av,2}$ |
|-----------|-------------------|-----------------|-------------------|-----------------|
| 1.1547    | -5.5346           | -6.7019         | -10.5026          | -12.0711        |
| 1.7321    | -7.9043           | -11.0792        | -13.2176          | -16.5852        |
| 2.0817    | -7.2731           | -7.6482         | -12.5287          | -13.0159        |
| 2.8868    | -8.2996           | -9.7492         | -13.6225          | -15.1359        |
| 3.0551    | -8.0970           | -8.6223         | -13.4115          | -13.9862        |
| 3.4641    | -8.8583           | -9.3227         | -14.1986          | -14.6905        |
| 3.7859    | -8.6589           | -9.2623         | -13.9943          | -14.6260        |
| 4.7258    | -8.9231           | -8.7407         | -14.2648          | -14.0952        |
| 5.0000    | -9.0172           | -9.0100         | -14.3603          | -14.3650        |
| 5.6862    | -9.1180           | -9.6429         | -14.4631          | -14.9990        |
| 6.4291    | -9.3049           | -9.8026         | -14.6521          | -15.1579        |
| 7.0946    | -9.5278           | -9.8566         | -14.8769          | -15.2111        |
| 7.3711    | -9.4074           | -9.5712         | -14.7556          | -14.9247        |
| 8.0829    | -9.5431           | -9.6167         | -14.8922          | -14.9698        |
| 8.3267    | -9.4921           | -9.6134         | -14.8409          | -14.9662        |
| 8.7369    | -9.6973           | -9.9986         | -15.0472          | -15.3518        |
| 9.8150    | -9.7037           | -9.8903         | -15.0536          | -15.2428        |
| 10.0167   | -9.6323           | -9.6926         | -14.9819          | -15.0447        |
| 10.1489   | -9.6717           | -9.7987         | -15.0215          | -15.1509        |
| 10.4403   | -9.7986           | -9.9958         | -15.1488          | -15.3481        |
| 10.6927   | -9.7210           | -9.8310         | -15.0709          | -15.1831        |
| 11.6762   | -9.7431           | -9.8290         | -15.0931          | -15.1809        |
| 11.8462   | -9.7469           | -9.8273         | -15.0970          | -15.1791        |
| 12.2202   | -9.8575           | -10.0860        | -15.2078          | -15.4379        |
| 12.4231   | -9.8141           | -10.0185        | -15.1643          | -15.3703        |
| 12.5033   | -9.8081           | -9.9754         | -15.1583          | -15.3272        |
| $\infty$  | -10.2838          |                 | -15.6327          |                 |

Kim, Nature 462, 196 (2009).

- <sup>8</sup> B. E. Feldman, J. Martin and A. Yacoby, Nature Physics 5, 889 (2009).
- <sup>9</sup> H. Min, G. Borghi, M. Polini and A. H. MacDonald, Phys. Rev. B **77**, 041407(R) (2008); Y. Barlas and K. Yang, Phys. Rev. B **80**, 161408(R) (2009); O. Vafeek and K. Yang, Phys. Rev. B **81**, 041401(R) (2010); F. Zhang, H. Min, M. Polini, and A. H. MacDonald, Phys. Rev. B **81**, 041402 (R) (2010); R. Nandkishore and L. Levitov, Phys. Rev. Lett. **104**, 156803 (2010); R. T. Weitz, M. T. Allen, B. E. Feldman, J. Martin and A. Yacoby, Science **330**, 812 (2010); J. Martin, B. E. Feldman, R. T. Weitz, M. T. Allen and A. Yacoby, Phys. Rev. Lett. **105**, 256806 (2010); R. T. Weitz, M. T. Allen, B. E. Feldman, J. Martin and A. Yacoby, arXiv:1010.0989 (2010).
- <sup>10</sup> J. Jung, F. Zhang and A. H. MacDonald, Phys. Rev. B **83**, 115408 (2011).
- <sup>11</sup> H. Min and A. H. MacDonald, Prog. Theor. Phys. Suppl. **176**, 227

- (2008);
- <sup>12</sup> M. Fujita, K. Wakabayashi, K. Nakada, K. Kusakabe, J. Phys. Soc. Jpn. **65**, 1920 (1996); J. Jung, T. Pereg-Barnea, and A. H. MacDonald, Phys. Rev. Lett. **102**, 227205 (2009).
- <sup>13</sup> A. A. Abrikosov and S. D. Beneslavskii, Zh. Eksp. Teor. Fiz. **59**, 1280 (1970) [Sov. Phys. JETP **32**, 699 (1971)].
- <sup>14</sup> J. Gonzalez, F. Guinea, and M. A. H. Vozmediano, Phys. Rev. B **59**, R2474 (1999); Phys. Rev. Lett. **77** 3589 (1996); Nucl. Phys. B **424**, 595 (1994); J. Low. Temp. Phys. **99**, 287 (1994). M. A. H. Vozmediano, M. P. Lopez-Sancho, T. Stauber, and F. Guinea, Phys. Rev. B **72**, 155121 (2005); F. Guinea, A.H. Castro Neto, and N.M.R. Peres, Eur. Phys. J. Special Topics **148**, 117 (2007).
- <sup>15</sup> Y. Barlas, T. Pereg-Barnea, M. Polini, R. Asgari, and A. H. MacDonald, Phys. Rev. Lett. **98**, 236601 (2007).
- <sup>16</sup> G. Borghi, M. Polini, R. Asgari and A. H. MacDonald, Solid State Comm. **149** 1117 (2009).
- <sup>17</sup> A. Bostwick, T. Ohta, T. Seyller, K. Horn and E. Rotenberg, Nature Physics **3**, 36 (2007); E. Rotenberg, A. Bostwick, T. Ohta, J. L. McChesney, T. Seyller and K. Horn, Nature Materials **7**, 258 (2008).
- <sup>18</sup> D. C. Elias, R. V. Gorbachev, A. S. Mayorov, S. V. Morozov, A. A. Zhukov, P. Blake, K. S. Novoselov, A. K. Geim, F. Guinea, arXiv:1104.1396v1 (2011).
- <sup>19</sup> J. E. Drut and T. A. Lähde, Phys. Rev. B **79**, 165425 (2009); A. H. Castro Neto, Physics **2**, 30 (2009).
- <sup>20</sup> S. Raghu, X.-L. Qi, C. Honerkamp, and S.-C. Zhang, Phys. Rev. Lett. **100**, 156401 (2008).
- <sup>21</sup> J. C. Slater and G. F. Koster, Phys. Rev. **94**, 1498 (1954).
- <sup>22</sup> H. Min, B. Sahu, S. K. Banerjee, and A. H. MacDonald, Phys. Rev. B **75**, 155115 (2007).
- <sup>23</sup> M. Zarea and N. Sandler, Phys. Rev. Lett. **99** 256804 (2007); R. Egger and A. O. Gogolin, Phys. Rev. Lett. **79**, 5082 (1997).
- <sup>24</sup> J. Alicea and M. P. A. Fisher, Phys. Rev. B **74**, 075422 (2006); Solid State Comm. **143**, 504 (2007); O. V. Yazyev, Phys. Rev. Lett. **101** 037203 (2008); S. Bhowmick and V. B. Shenoy, J. Chem. Phys. **128**, 244717 (2008); B. Wunsch, T. Stauber, F. Sols, and F. Guinea, Phys. Rev. Lett. **101**, 036803 (2008).
- <sup>25</sup> T. O. Wehling, E. Şaşıoğlu, C. Friedrich, A. I. Lichtenstein, M. I. Katsnelson, and S. Blügel, arXiv:1101.4007 (2011).
- <sup>26</sup> S. Dutta, S. Lakshmi, and S. K. Pati, Phys. Rev. **77**, 073412 (2008).
- <sup>27</sup> C. Jang, S. Adam, J.-H. Chen, E. D. Williams, S. Das Sarma, and M. S. Fuhrer, Phys. Rev. Lett. **101**, 146805 (2008).
- <sup>28</sup> P.R. Wallace, Phys. Rev. **77**, 622 (1947).
- <sup>29</sup> G. E. Volovik, 'The Universe in a Helium Droplet', Oxford University Press (2003).
- <sup>30</sup> I. M. Tsidilkovski, in *Electron Spectrum of Gapless Semiconductors*, edited by Klaus von Klitzing, Springer Series in Solid-State Sciences Vol. 116 (Springer, New York, 1996) and references therein.
- <sup>31</sup> See for example L. Sosnowsky or E. O. Kane in Lecture Notes in Physics **133**, *Narrow Gap Semiconductors Physics and Applications*, Ed. W. Zawadzki, Springer-Verlag (1980);
- <sup>32</sup> B. I. Halperin and T. M. Rice, Rev. Mod. Phys. **40**, 755766 (1968).
- <sup>33</sup> B. L. Gel'mont, Fiz. Tekh. Poluprovodn., **9** (1975), 1912; [Sov. Phys. Semicond., **9** (1975), 1257].
- <sup>34</sup> L. Liu and D. Brust, Phys. Rev. Lett. **20**, 651 (1968); L. Liu and D. Brust, Phys. Rev. **173**, 777 (1968).
- <sup>35</sup> A. A. Abrikosov and S. D. Beneslavskii, J. Low Temp. Phys., Vol. **5**, No. 2, (1971).
- <sup>36</sup> G. F. Giuliani and G. Vignale, *Quantum Theory of the Electron Liquid*, Cambridge University Press, Cambridge, 2005.
- <sup>37</sup> M. Fujita, K. Wakabayashi, K. Nakada, K. Kusakabe, J. Phys. Soc. Jpn. **65**, 1920 (1996);

- <sup>38</sup> S. Sorella and E. Tosatti, *Europhys. Lett.* **19**, 699 (1992); L. M. Martelo, M. Dzierzawa, L. Siffert, and D. Baeriswyl, *Z. Phys. B* **103**, 335 (1997).
- <sup>39</sup> T. Paiva, R. T. Scalettar, W. Zheng, R. R. P. Singh, and J. Oitmaa, *Phys. Rev. B* **72** 085123 (2005).
- <sup>40</sup> Z. Y. Meng, T. C. Lang, S. Wessel, F. F. Assaad, and A. Muramatsu, *Nature* **464**, 847 (2010); *High Performance Computing in Science and Engineering '10*, Part 1, 5-17, Springer (2011).
- <sup>41</sup> I. F. Herbut, *Phys. Rev. Lett.* **97**, 146401 (2006); I. F. Herbut, V. Juricic, B. Roy, *Phys. Rev. B* vol. **79**, 085116 (2009); V. Juricic, I. F. Herbut, G. W. Semenoff, *Physical Review B* **80**, 081405 (R) (2009).
- <sup>42</sup> M. Z. Hasan and C. L. Kane, *Rev. Mod. Phys.* **82**, 3045 (2010).
- <sup>43</sup> R. Saito, M. Fujita, G. Dresselhaus, M. S. Dresselhaus, *Appl. Phys. Lett.* **60**, 2204 (1992).
- <sup>44</sup> J. Jung and A. H. MacDonald, *Phys. Rev. B* **80**, 235417 (2009).
- <sup>45</sup> N. H. Shon and T. Ando, *J. Phys. Soc. Jpn.* **67**, 2421 (1998).
- <sup>46</sup> J. P. Reed, B. Uchoa, Y. I. Joe, Y. Gan, D. Casa, E. Fradkin and P. Abbamonte, *Science* **330**, 805 (2010).
- <sup>47</sup> P. P. Ewald, *Ann. Phys.*, **64**:253, (1921).
- <sup>48</sup> P. J. Steinbach and B.R. Brooks. *J. Comp. Chem.*, **15**:667, (1994).
- <sup>49</sup> M. Polini, R. Asgari, Y. Barlas, T. Pereg-Barnea, A.H. MacDonald *Solid State Commun.* **143**, 58 (2007).
- <sup>50</sup> S. Das Sarma, E. H. Hwang, and Wang-Kong Tse, *Phys. Rev. B* **75**, 121406(R) (2007).